Increased rainfall in southern Central America under glacial climate conditions

Elise Luciani, Guillaume Leduc, Yannick Garcin, Frauke Rostek, Kazuyo Tachikawa, Marta Garcia, Masa Kageyama, Edouard Bard

Elise Luciani, Guillaume Leduc, Yannick Garcin, Frauke Rostek, Kazuyo Tachikawa, et al.. Increased rainfall in southern Central America under glacial climate conditions. Earth and Planetary Science Letters, 2025, 672, pp.119699. ⟨10.1016/j.epsl.2025.119699⟩. ⟨hal-05357243⟩

HAL Id: hal-05357243
https://amu.hal.science/hal-05357243v1

Submitted on 10 Nov 2025

Increased rainfall in southern Central America under glacial climate conditions

Elise Luciani[1*], Guillaume Leduc[1], Yannick Garcin[1], Frauke Rostek[1], Kazuyo Tachikawa[1], Marta Garcia[1], Masa Kageyama[2], Edouard Bard[1]

[1]: Aix Marseille Univ, CNRS, IRD, INRAE, Coll France, CEREGE, Aix-en-Provence, France

[2]: LSCE/IPSL, UMR CEA-CNRS-UVSQ 8212, Université de Paris-Saclay, 91190, Gif-sur-Yvette, France

*: corresponding author: (luciani@cerege.fr)

Abstract

Late Pleistocene hydroclimate variability in Central America and its associated climate forcings are poorly constrained. The region is influenced by complex ocean-atmosphere-continent interactions, and documented palaeohydrological responses, which vary by site and/or proxy specificity, are far from conclusive. We used δD of n-alkanes from a marine sediment core in the Panama Basin to infer past changes in precipitation over the last 56 kyr. Our results indicate a progressive intensification of precipitation during the last glacial period, culminating in a precipitation maximum during the Last Glacial Maximum (LGM, 23-19 kyr BP), followed by a rapid decline during the Heinrich Event 1 (H1, 18-15 kyr BP) time interval. While the regional pattern of the precipitation anomaly during the LGM is proxy and site dependent, the regional drying during H1 shows a clear north-south signature associated with the southward meridional migration of the Intertropical Convergence Zone

(ITCZ). Using iTrace and PMIP4 model simulations, we show that the precipitation changes associated with the ITCZ shift are closely linked to the equatorial SST front induced by changes in the oceanic circulation. We propose that an increase in this latitudinal SST gradient could have locally pushed the ITCZ further north, bringing rainfall to southern Central America during the LGM.

Keywords:

plant waxes isotopic composition, hydroclimate, Last Glacial Maximum, Central America, Intertropical Convergence Zone, ocean-atmosphere interactions

1 Introduction

Tropical regions, where the highest total rainfall occurs, host more than half of the world's population. However, tropical rainfall is one of the most difficult parameters to simulate with climate models (Douville et al., 2021). Atmospheric convection and its associated rainfall occur above the warmest regions in the tropical ocean realm, so that any change in the regional pattern of the tropical warm pools could have a profound impact on regional rainfall (Tierney et al., 2013).

Warm pools are specific areas in the global ocean where the sea surface temperature (SST) remains above 28.5°C throughout the year. Around the equator, three high precipitation hotspots develop above the warm pools, located over Central America, the Indonesian region and equatorial Africa (Trenberth and Shea, 2005). These precipitation maxima are associated with large-scale meridional and zonal atmospheric structures that vary on seasonal and interannual scales (Schneider et al., 2014). Central America lies at the core of the Western Hemisphere Warm Pool (WHWP), which is divided into two oceanic regions: the Eastern Pacific Warm Pool (EPWP) and the Atlantic Warm Pool. Central America makes the WHWP span two oceans and sets up complex regional interactions between land, atmosphere and ocean processes.

These characteristics make it difficult to assess the regional response of precipitation to global climate change in the WHWP. For example, palaeoclimatic simulations of the Last Glacial Maximum (LGM) provide contrasting hydroclimatic conditions in the WHWP region, as the sign of LGM precipitation changes are model-dependent (Kageyama et al., 2021). Globally, the ITCZ is thought to have migrated towards the warmest hemisphere above oceans, with latitudinal shifts of about 1° during the LGM and with a notable additional southward shift during Heinrich Event 1 (H1, McGee et al., 2014), while terrestrial precipitation responds thermodynamically to monsoon systems occurring over continental landmasses (Singarayer et al., 2017).

Reconstructions of tropical rainfall dynamics and the associated meridional position and/or expansion of the ITCZ have led to alternating interpretations, leading to an unclear picture of palaeoprecipitation evolution in the tropical American region. Regionally, Rincón-Martínez et al. (2010) reported a northward shift of the ITCZ in the eastern equatorial Pacific (EEP) for the LGM relative to today, while Arbuszewski et al. (2013) reported a southward shift of the ITCZ in the equatorial Atlantic. However, these records are located far from the WHWP, and other records from the area are either salinity based and provide contrasting results (**Figure S1**), or do not cover the entire last glacial termination (Lachniet et al., 2009).

The aim of this study is to assess the spatial patterns of precipitation variability in Central America during the LGM and to identify the climatic drivers of these precipitation patterns. We present a precipitation reconstruction of Central America by analysing plant wax from a marine sediment core collected in the Panama Basin, which traces changes in precipitation over the adjacent continent over the last 56 kyrs. The MD02-2529 core is ideally located in the WHWP, an area where records of LGM and deglacial atmospheric hydroclimate are lacking. Our results provide insights into the past hydroclimatic cycle of Central America, which we explain by analysing PMIP4 model simulations of the LGM (Kageyama et al., 2021). We identify an ocean-atmosphere interaction in the EEP, where the latitudinal SST gradient drives rainfall changes in the warm pool region.

2 Regional climatology

MD02-2529 was collected in the EEP 08°12.33' N, 84°07.32' W, 1619 m water depth (Beaufort et al., 2002). The surface waters of the EEP are characterised by two strong gradients in sea surface temperature (SST). The northern EEP is characterised by warm and stratified surface waters as part of the Eastern Pacific Warm Pool (EPWP), which extends along the coast of central Mexico to Nicaragua with SST warmer than 28.5°C (**Figure 1**). This EPWP is the Pacific part of the larger WHWP, which includes the EPWP, the Caribbean Sea and part of the Gulf of Mexico (Wang & Enfield, 2001). Further south, a strong front separates the EPWP from the colder waters of the equatorial cold tongue (**Figure 1d**). The equatorial front is one of the steepest SST gradients in the world. The spatial and temporal variations in precipitation are mainly driven by changes in the SST patterns in the EEP, which influence the regional wind stress convergence (Chelton, 2001) and the resulting ITCZ.

At the seasonal scale, precipitation patterns in southern Central America are characterised by a dry season during the boreal winter and a wet season during the boreal summer (**Figure 1**), resulting from the latitudinal shift of the ITCZ (**Figure 1c, f**). The wet season is interrupted in July during the midsummer drought, resulting in a bimodal wet season with two precipitation maxima in May-June and September-October (**Figure 2a**).

Interbasin changes in the SST pattern also influence moisture transport across the isthmus from the Atlantic to the Pacific (Leduc et al., 2007). The Caribbean low-level jet (**Figure S2a**), a trade wind that originates in the Atlantic and is mainly active from June to August (Amador et al., 2006), is the main moisture conveyor across the isthmus (Durán-Quesada et al., 2010).

The low-level circulation also consists of the Choco low-level jet, a westerly wind that blows along the Peruvian coast and changes direction as it crosses the equator, bringing moisture to the isthmus from September to November (Poveda and Mesa, 2000, **Figure S2b**). On an interannual timescale, the El Niño Southern Oscillation (ENSO) is the main mode of SST variability in the EEP and drastically affects the cold tongue region (Rasmusson and Carpenter, 1982). El Niño warm events manifest as a precipitation deficit in the Pacific region and as a precipitation intensification in the Caribbean region (Sánchez-Murillo et al., 2017). However, along the Costa Rican margin, El Niño years only slightly alter the annual cycle of rainfall rates and their isotopic composition (Linsley et al., 1994).

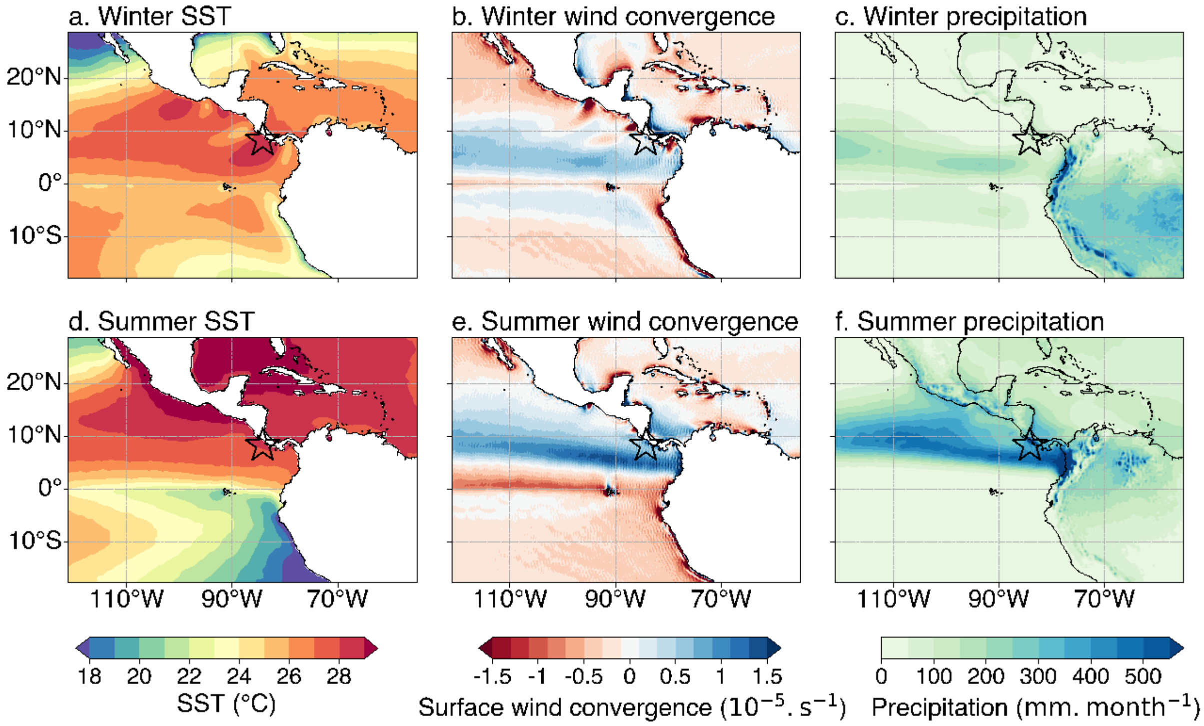

Figure 1. Modern climatology of Central America and adjacent Eastern Equatorial Pacific ocean. **a, d:** SST (°C); **b, e:** Surface wind convergence ($10^{-5}.s^{-1}$); **c, f:** Precipitation rates (mm.month^{-1}) for boreal winter (January, February, March, upper panels) and summer (July, August, September, lower panels). The star indicates the position of core MD02-2529. Data from ERA5 (Hersbach et al., 2023).

3 Material and Methods

3.1 Chronology

The chronology for core MD02-2529 has been modified from Leduc et al. (2007), in particular with the addition of three radiocarbon dates for the Holocene time window indicating a mislabelled section on board during the MONA cruise (see Supplementary Text 1 and **Figure S3**).

We now have fourteen radiocarbon dates for the planktonic foraminiferal species *Neogloboquadrina dutertrei*. Of these fourteen radiocarbon dates, two were separated by only 1 cm in the sedimentary sequence and gave virtually the same age (Leduc et al., 2007); we therefore merged these two radiocarbon dates for the final age model, which contains thirteen radiocarbon-based age control points (**Table S1**). We used the Bacon package on R software (Blaauw and Christen, 2011, **Figure S4**) to calibrate radiocarbon ages against the Marine20 radiocarbon calibration curve (Heaton et al., 2020), taking into account the local reservoir age ΔR of -72 ± 94 yr for the surface water mass at the core site (http://calib.org/marine/). To obtain additional age control points beyond the radiocarbon age limit, we used isotope stratigraphy as described in Leduc et al. (2007), but with the updated Greenland and Antarctic ice core timescales GICC05 published in Svensson et al. (2020).

3.2 *n*-alkanes extraction and quantification

Total lipids were extracted from 5 to 10 g of freeze-dried sediment using an Accelerated Solvent Extractor (ASE 350, Thermo Scientific), with a dichloromethane/methanol mixture of 9:1. Known amounts of squalane and C_{36} *n*-alkane were added prior to extraction as internal standards. Total lipid extracts (TLE) were eluted with hexane on silica gel column chromatography yielding the apolar (F1) fraction including *n*-alkanes. F1 was then purified on an Ag-Si column with hexane. *n*-alkanes were quantified by comparing the integrated peak areas with those of the C_{36} *n*-alkane internal standard using a Thermo Scientific Trace GC gas chromatograph (GC) equipped with a DB-5-MS (J&W) column (60 m x 0.25 mm x 0.1 µm) fitted with a 2.5 m x 0.53 µm deactivated retention gap, using hydrogen as a carrier gas and a flame ionization detector (FID).

3.3 Compound-specific carbon and hydrogen stable isotope analysis

Compound-specific stable hydrogen (δD) and carbon isotope ($\delta^{13}C$) analysis of long chain *n*-alkanes was performed at CEREGE on a Thermo Scientific Trace GC coupled via a GC Isolink II conversion unit to a Thermo Fisher Scientific Delta V^+ mass spectrometer. The GC was equipped with a TG5ms (30 m × 0.25 mm x 0.25 µm column) and Helium was used as the carrier gas. The GC temperature was programmed to increase from 80°C to 180°C at 10°C/min and then at 5°C/min to 315°C (held 16 min). The HTC pyrolysis reactor was held at 1420°C for hydrogen analysis and the combustion reaction was held at 1000°C for carbon analysis.

The samples were injected in random stratigraphic order in duplicate. Due to low concentrations of sedimentary *n*-alkanes, around 30% of the data produced mass spectrometer signals below 2 V and were excluded. Nonetheless, the C_{29} and C_{31} *n*-alkane homologues exhibit almost identical δD variations, despite having different abundances, suggesting that the isotopic signal as a whole is not impacted by small amounts of *n*-alkanes.

Instrument performance and the H_3^+ factor were monitored on a daily basis using a reference H_2 gas and a mixture of n-alkanes of known isotopic composition. The H_3^+ factor (Sessions et al., 2001) was 5.5 ± 0.09 during the analysis period. The *n*-alkane mixture A7 (provided by Arndt Schimmelmann; Indiana University) was used as an external standard mixture. It was analysed in duplicate repeatedly every six injections to monitor potential deviation throughout a sequence of analysis and the entire period of analysis. Additional injections of an internal sedimentary standard (from Lake Chad) were also monitored for each sequence of analysis.

All the A7 mix, Lake Chad and the squalane recovery standard indicate a standard deviation of δD and $\delta^{13}C$ better than 2 ‰ and 0.4 ‰, respectively. δD and $\delta^{13}C$ are given in ‰ relative to Vienna Standard Mean Ocean Water (V-SMOW) and Vienna Pee Dee Belemnite (V-PDB), respectively.

3.4 PMIP4 models

We have used the available model results from the latest generation of PMIP experiments (PMIP4; Kageyama et al., 2021), most of which are part of the Coupled Model Intercomparison Project phase 6 (CMIP6). The database now also includes CESM2.1 (Zhu et al., 2021a), which has been processed like all other models published in Kageyama et al. (2021). The LGM model outputs analysed here are from the PMIP4-CMIP6 LGM experiments (Kageyama et al., 2017). We use the corresponding pre-industrial (PI) control experiments as a reference. The LGM boundary conditions differ from those of the PI period mainly due to reduced atmospheric concentrations of greenhouse gases, lower sea level, the presence of large continental ice sheets and an orbital configuration set at 21 kyr BP (Kageyama et al., 2017).

SST and total precipitation data from 13 different models were obtained from the CMIP6 ESGF database and the PMIP4 database (http://dods.lsce.ipsl.fr/pmip4/db/). The 13 models using the PMIP4 protocol are the 12 models UofT-CCSM4, MIROC-ES2L, HadCM3 ICE-6G, HadCM3 GLAC-1D, CESM1.2, AWIESM1, AWIESM2, INM-CM4-8, iLOVECLIM GLAC-1D, iLOVECLIM ICE-6G, MPI-ESM1.2 and IPSL-CM5A2 presented in Kageyama et al. (2021) and the CESM2.1 simulation from Zhu et al. (2021a). We defined large enough geographical areas to compute regional averages that are representative of the regions of interest. We delimited two SST regions for the calculation of latitudinal SST gradients in the EEP, i.e. the cold tongue (5°S-0°, 93°W-83°W) and the EPWP (7°N-12°N, 97°W-87°W), and two precipitation regions for the detection of latitudinal shifts in the ITCZ (0°N-5°N, 95°W-85°W and 8°N-13°N, 95°W-85°W, see red and black rectangles in **Figure 6**). The southern ITCZ position corresponds to the southernmost position of the modern ITCZ (**Figure 1c**) and the northern ITCZ position corresponds to the northernmost position of the modern ITCZ (**Figure 1f**). To keep the calculations consistent, we have chosen a fixed location of these geographical areas to calculate the gradients of SST and precipitation for all models, even though the reproduction of these zonal patterns can vary between models by a few degrees of latitude. In addition to oceanic and climatic variability, averaging the boxes used to calculate the model-derived sea surface temperature (SST) and precipitation gradients mitigates disparities in the spatial resolution of the different models.

3.5 iTrace simulation

The iTrace simulation is a transient simulation covering the period from 20 to 11 kyr BP (He et al., 2021, data available at https://doi.org/10.26024/b290-an76). It uses iCESM1.2, an isotope-enabled coupled GCM (Brady et al., 2019) with the control experiments iCESM1.3 LGM and PI from Zhu et al. (2017). We use the iTrace core experiment version, which includes the evolving orbital conditions, ice sheets, greenhouse gases and meltwater of the run (He et al., 2021).

The iCESM1.3 PI control and LGM experiments reproduce the seasonal cycle of precipitation rates and the amount effect on precipitation δD, albeit without the mid-summer dry season and with an anomalously low magnitude of seasonal δD changes (**Figure 2**).

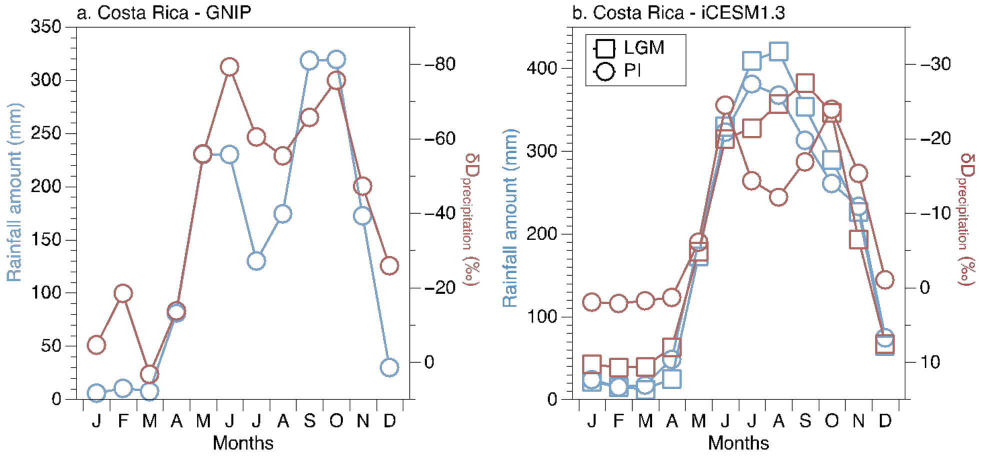

Figure 2. Modern climatology over Costa Rica in GNIP data and comparison with iCESM1.3 (iTRACE control experiment). (a) Monthly precipitation amount (mm.month^{-1}) and associated δD of precipitation (‰) in Costa Rica. Monthly GNIP data from Heredia station in Costa Rica averaged during the 2013-2020 period (IAEA/WMO, 2024). (b) iCESM1.3 (Zhu et al., 2017) precipitation amount (mm.month^{-1}) and δD of precipitation (‰) in Costa Rica (at 8.5°N, 82.5°W) for the PI control simulation (circles) and the LGM simulation (squares). Note the difference in y scaling in a and b because the magnitude of the δDprecipitation seasonality in the iCESM1.3 model is damped compared to the GNIP isotopic data.

4 Results

4.1 *n*-alkane concentrations

Plant wax long chain n-alkanes are derived from the epicuticular waxes of terrestrial higher plants (see e.g. Sachse et al., 2012). The average sedimentary concentrations of the four dominant long-chain odd-numbered *n*-alkanes of core MD02-2529 are approximately 80, 300, 320 and 170 ng.g^{-1} for *n*-C_{27}, *n*-C_{29}, *n*-C_{31} and *n*-C_{33}, respectively (**Figure 3a**). The two most abundant are *n*-C_{29} and *n*-C_{31}, which vary from a minimum of 25 ng.g^{-1} to a maximum of 830 ng.g^{-1} for *n*-C_{29} and from 27 ng.g^{-1} to 920 ng.g^{-1} for *n*-C_{31} (**Figure 3a**).

All homologues share the same temporal trends, with maximum and minimum abundances recorded during the LGM and the Holocene, respectively (**Figure 3a**). There is a marked decrease in *n*-C_{29} and *n*-C_{31} concentrations between ~ 18 and 15 kyr BP, coeval with the Heinrich event 1 chronozone. Conversely, the other Heinrich events that punctuated the MIS 3 period are not apparent in the *n*-alkane concentration changes.

4.2 δ^{13}C of *n*-alkanes

C_3 and C_4 physiological pathways lead to different δ^{13}C values of plant wax. A recent literature review reports n-alkane δ^{13}C values for C_3 vegetation in tropical rainforest environments of ~-35 to -40 ‰ and values for C_4 grass of ~-20 to -23 ‰ (Liu et al., 2022).

MD02-2529 *n*-C29 and *n*-C31 δ^{13}C records vary from -35.0 ‰ to -31.7 ‰ (-33.8 ‰ on average) and from -35.6 ‰ to -31.7 ‰ (-33.7 ‰ on average), respectively, without any noticeable long-term trend (**Figure 3b**). These *n*-C29 and *n*-C31 values clearly indicate that the vegetation type was predominantly a rainforest for the entire time interval studied (**Figure 3b**).

Changes in the relative proportion of the respective contributions of *n*-alkanes synthesised by C_3 versus C_4 plants can also obscure the plant wax δD signal because both C_3 and C_4 physiological pathways do not have the same magnitude of apparent fractionation between the isotopic signatures of water and plant wax (McInerney et al., 2011). The constant δ^{13}C values exclude the need to correct the δD values for changes in vegetation types that may have altered the δD signal. We will assume that there is no variation in the C_3 and C_4 photosynthetic pathways of the plant types producing the analysed sedimentary plant waxes and interpret the δD changes of the plant waxes as reflecting those associated with the δD of environmental water.

4.3 δD of *n*-alkanes

n-C_{29} and *n*-C_{31} δD records vary from -166 to -141 ‰ (-154 ‰ on average) and from -166 to -142 ‰ (-157 ‰ on average), respectively (**Figure 3c**). The isotopic δD compositions of the two homologues exhibit the same temporal changes, with a long-term progressive isotopic decrease for the 56-18 kyr BP time window, a subsequent sharp isotopic increase of about 20 ‰ co-occurring during the Heinrich event 1 chronozone, and a Holocene period marked by the highest δD values during which we observe some multi-millennial δD fluctuations (**Figure 3c**).

We corrected our δD *n*-alkane data from the global isotope changes in the water cycle on a glacial-interglacial scale with the δ^{18}O isotope values in Waelbroeck et al. (2002) with the following conversion: $\delta D_{n\text{-alkane ivc}}=8*\delta^{18}O*(1+\delta D_{n\text{-alk}}/1000)/(1+8*\delta^{18}O/1000)$ (**Figure 3d**). We interpret the ice-volume corrected δD of *n*-alkanes ($\delta D_{\text{n-alkane ivc}}$) as a proxy for the δD of environmental water (Sachse et al., 2012). Once applied, the correction does not significantly reshape the changes observed in the raw $\delta D_{n\text{-alkane}}$, indicating that changes in ice volume have only a secondary effect on $\delta D_{n\text{-alkane}}$.

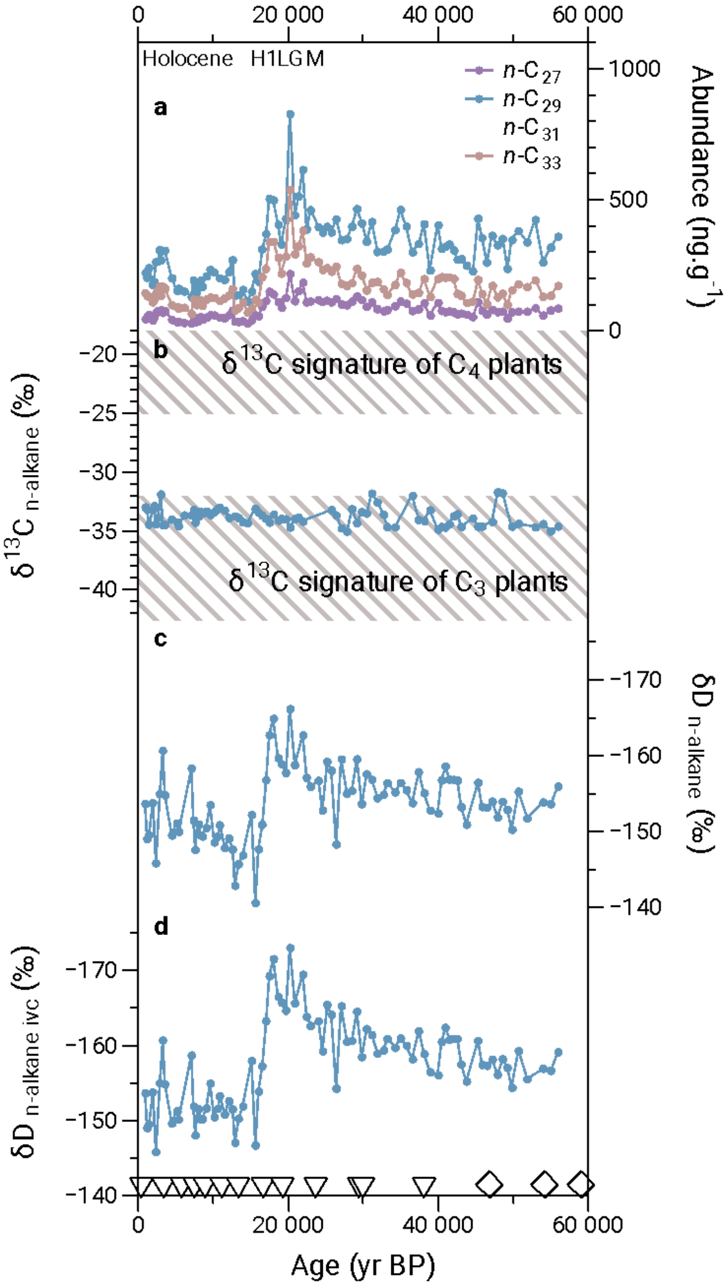

Figure 3. MD02-2529 *n*-alkanes analysis. (a) Abundance of the four dominant *n*-alkanes, (b) $\delta^{13}C$ *n*-C_{29} and *n*-C_{31}, hatched areas represent the range of both C_3 and C_4 *n*-alkanes tropical

carbon isotopic signatures (Liu et al., 2022), (c) δD n-C_{29} and n-C_{31} values, and (d) δD n-C_{29} and n-C_{31} values corrected for ice volume changes. The age control points are displayed as triangles (radiocarbon dating) and diamonds ($\delta^{18}O$ tie points).

5 Discussion

5.1 Control on the plant wax sources

Eolian, fluvial, and marine processes transport and deposit *n*-alkanes into the Panama Basin sediments. Spatial distribution of multiple biomarkers of terrestrial origin in the Panama Basin marine sediments indicate that river discharge is the main mode of transport of *n*-alkanes at coring site (see Huguet et al., 2019 for discussion). We hypothesize that MD02-2529, currently located 60 km away from the continent where tropical forests dominate continental vegetation, are influenced by fluvial inputs of terrestrial organic matter. $\delta^{13}C$ values of *n*-alkanes are in agreement with those from the tropical forest vegetation in Costa Rica (Douglas et al., 2012). As there is no influence of lateral advection on *in-situ* oceanic biomarkers (e.g. alkenones) in the Panama Basin (Kusch et al., 2010), we suppose negligible lateral transport of previously deposited continental biomarkers that could overprint syn-deposited *n*-alkanes.

Given that the measured wet bulk density is nearly constant downcore of MD02-2529 (Beaufort, 2002), that the carbonate, opal and organic carbon content is always below 15, 5 and 4% respectively (Leduc et al., 2010; Romero et al., 2011) and that sedimentation rate changes smoothly from the mid-Holocene to the core bottom, we attribute the changes in *n*-alkane concentration to changes in *n*-alkane fluxes mediated by wet transport from the adjacent continent without significant changes in dilution by biogenic remains (**Figure S5**). Even if MD02-2529 is only located 60 km away from the coast, the local continental margin is so narrow that we could exclude significant changes in the distance of the marine core to the coast during glacial periods to explain the increases in the *n*-alkane fluxes at coring site

(Harris et al., 2013). We thus directly interpret the *n*-alkane concentrations as reflecting the intensity of *n*-alkanes delivery by regional riverine runoff.

5.2 Controls on the water isotopic signal recorded by terrestrial plant *n*-alkanes

Leaf waxes ultimately record environmental water during biosynthesis before being fossilised in sedimentary sequences, and δD in lipid biomarkers thus record the isotopic composition of environmental water (Sauer et al., 2001), influenced by evaporation-precipitation processes and specific biosynthetic fractionations during lipid biosynthesis (Sachse et al., 2012). On a global scale, there is a direct relationship between the δD of n-alkanes and the δD of mean annual precipitation (Sachse et al., 2012; Ladd et al., 2021).

In the tropics, the primary control on water isotopic composition of precipitation is the amount effect (**Figure 2**), which corresponds to a negative relationship between precipitation amount and the isotopic composition of precipitation (Dansgaard, 1964; Risi et al., 2008). However, other processes such as cloud microphysics (Konecky et al., 2019), types of precipitation (e.g. stratiform vs. convective, Aggarwal et al, 2016; Konecky et al., 2019), strength of deep convection (Tharammal et al., 2017), origin and transport of moisture (Sánchez-Murillo et al., 2016) can all affect the isotopic signal of precipitation. Regionally, monthly isotopic values of precipitation in Belize, Guatemala (Lachniet and Patterson, 2009) and Costa Rica (Sánchez-Murillo et al., 2013) indicate a primary influence of the amount effect, with a secondary influence of the origin of moisture sources (Lachniet et al., 2007). El Niño warm events do not exhibit any significant alteration in the monthly relationship between isotope and precipitation amount (Sánchez-Murillo et al., 2017).

We hence interpret changes in $\delta D_{\text{n-alkane ivc}}$ in MD02-2529 as reflecting changes in precipitation rate, with wetter (more negative δD) versus drier conditions (less negative δD) in southern Central America.

5.3 Regional rainfall changes in Central America

Spatiotemporal changes in precipitation patterns are alternatively explained either by a continental monsoon system associated with seasonal alternations of sea-land pressure contrasts and their associated wind reversal, or by the seasonal latitudinal migration of the ITCZ that mainly manifests above the warmest tropical ocean regions (Geen et al., 2020). Global monsoon characterises tropical precipitation areas with strong seasonal contrasts and a resulting wet season, whereas the ITCZ mainly tracks convective atmospheric variability responsible for a narrow latitudinal band of particularly intense precipitation rates over oceans (Geen et al., 2020).

In Central America, most of the climate forcings for the last glacial-interglacial transition have already been used to explain past changes in precipitation, because the timing of precipitation changes varied considerably in different subregions. In core MD02-2529, we record a slight increase in precipitation in Costa Rica from 60 to 18 kyr BP, without much variation during the glacial period, and with a dominant wet LGM. Precipitation decreases during the H1 event and remains low during the Holocene compared to the LGM, with additional multi-millennial variations. δD *n*-alkanes in the MD02-2529 core do not show a strong response to local or high latitude insolation at the orbital scale. In the following discussion, we focus on the major changes in the MD02-2529 record for the LGM and H1, and compare them with regional palaeorecords of precipitation in a broader context (**Figure 4**, **Figure 5, Figure S6**). In particular, we focus on a region that extends beyond Central America to include the Caribbean and northern South America.

5.3.1 LGM

Comparison of the LGM with the late Holocene isotopic record indicates a wetter LGM in MD02-2529 (**Figure 4 e**) and Caracos cave in Colombia (Ramirez et al., 2023, **Figure 4 f**), a slightly wetter than late Holocene LGM in SW Mexico (Lachniet et al., 2013, **Figure 4 c**), and a drier than present-day LGM in NE Mexican, Cuban caves (Wright et al., 2023; Warken et al., 2019, **Figure 4 a and b**) and Maya highlands caves (Lucia et al., 2024, **Figure 4 d**). It highlights contrasting glacial-interglacial changes in precipitation intensity with respect to latitude.

Interestingly, at Petén Itzá, Guatemala, the isotopic changes mimic those recorded in the northern Mexican caves, but other proxies for rainfall all show different rainfall changes (**Figure S6**). The first downcore record from Petén Itzá reported a wet LGM based on downcore magnetic susceptibility and sediment density (Hodell et al., 2008). A wetter LGM is further supported by isotopic and non-isotopic records, including pollen and diatom assemblages (**Figure S6**). This suggests that the contrasting proxies analysed at Petén Itzá have their own specificities and may preferentially record contrasting seasons, rainfall regimes and/or other aspects of these sedimentary sequences.

5.3.2 H1 event

MD02-2529 δD *n*-alkanes is characterized by a wet-to-dry transition during the H1 event (**Figure 3**). In all other isotopic records, the H1 event represents a dry climatic anomaly (**Figure 4**). Other non-isotopic records suggest such a pattern, and the only record indicating wetter conditions is located just south of the equator along the Pacific coast (Rincón-Martínez et al., 2010, **Figure 5**).

In high-resolution records from the North Atlantic, the H1 event has two phases (Bard et al., 2000). Some sites in tropical North America and the EEP also show multiple phases during H1 (**Figure S7**). Some numerical studies investigating ocean-ice sheet interactions during Heinrich events illustrate the complex processes likely to occur during Heinrich events (Alvarez-Solas et al., 2010). However, the MD02-2529 *n*-alkane record does not allow us to further investigate the complexity of the hydroclimate response of southern Central America during the H1 event due to the resolution and additional uncertainties associated with the changing reservoir age over time in the EEP (see, e.g., Zhao & Keigwin, 2018).

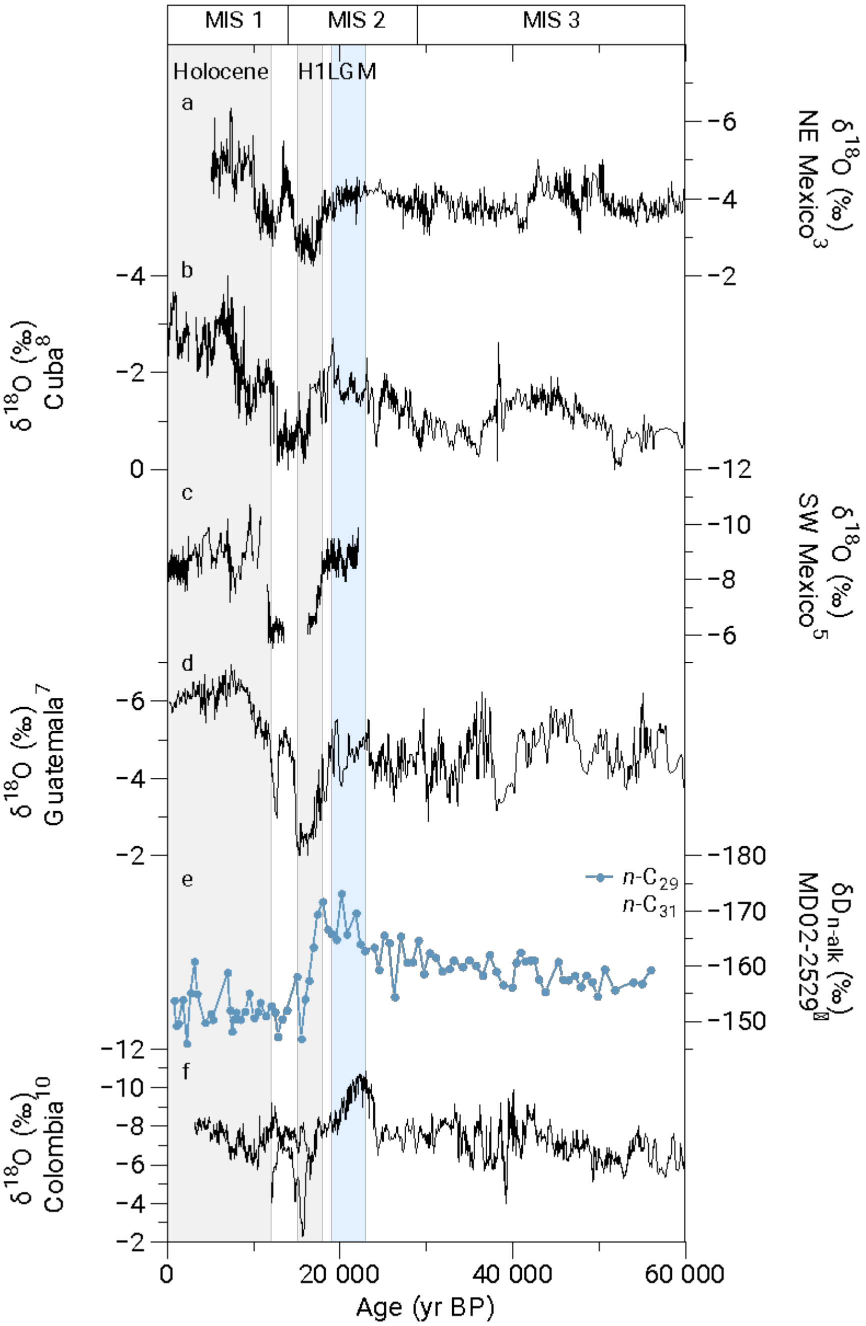

Figure 4. Comparison of (e) MD02-2529 δD *n*-alkanes ice volume corrected over the last 60 kyr with hydroclimate records in tropical America based on isotopic records. Speleothem $\delta^{18}O$ values in (a) Cueva Bonita, Mexico (Wright et al., 2023), (b) Santo Tomas cave and Dos Anas cave (Warken et al., 2019 and reference therein), Cuba ; (c) Juxtlahuaca cave and Cueva del Diablo (Lachniet et al., 2013 and reference therein), Mexico; (d) Maya highlands caves

(Grutas del Rey Marcos, Bombil Pek, and Jul Iq), Guatemala (Lucia et al., 2024 and reference therein); (f) Caracos cave, El Peñon, Colombia (Ramirez et al., 2023). All isotopic records are corrected for ice volume changes. Numbers associated with site labels are reported on the map in **Figure 5**.

5.3.3 Model-data comparison using the iTrace modeling simulation

The full iTrace simulation (He et al., 2021) allows us to consider the LGM-PI and LGM-H1 anomalies to investigate the spatial diversity of precipitation patterns and associated water isotope values. iTrace reproduces the LGM-PI anomaly over the continent near the coring site both in δD of precipitation (more negative δD *n*-alkanes in the record during the LGM and more negative δD precipitation in iCESM, **Figure 5a**) and in precipitation (**Figure 5b**). The iTrace simulation also reproduces the LGM-H1 anomaly of the MD02-2529 δD *n*-alkanes over the continent in both δD of precipitation (**Figure 5c)** and precipitation (**Figure 5d**). These results are consistent with the tropical response to Heinrich events (Bradley and Diaz, 2021) and the southward shift of the ITCZ due to North Atlantic cooling.

Spatial comparisons between δD precipitation and precipitation rate agree in the sign of the LGM-H1 anomaly (**Figures 5a and 5b**) over continental Central America, with more negative δD where LGM precipitation is higher than H1 precipitation. The LGM-PI anomaly (**Figure 5a and 5b**) is less pronounced than the LGM-H1 anomaly (**Figure 5c and 5d**), but the δD precipitation is still consistent with the sign of the changes, although not in magnitude when comparing the iCESM model and our data. Both isotopic anomalies (**Figures 5a and 5c**) and hydroclimate interpretations (**Figures 5b and 5d**) agree with the sign of change between LGM and PI (**Figure 5a and 5b**) and LGM and H1 (**Figure 5b and 5d**) iTrace model simulation.

5.4 A mechanism for a wet LGM in southern Central America

5.4.1 Ocean-atmosphere mechanism

Oceanic features influence atmospheric circulation above the EEP and the adjoining continent. Increasing atmospheric temperatures make their water-holding capacity increase. At the coring site, summer winds crossing the equator blow over the cold tongue SST gradient before converging above the Panama Basin where both SST and the air reaches temperatures much higher than those found in the cold tongue and further South (**Figure 1**). Eventually, wind convergence occurs at around 5°N downwind of the SST front, and convergence maxima co-occur with that of precipitation (**Figure 1**).

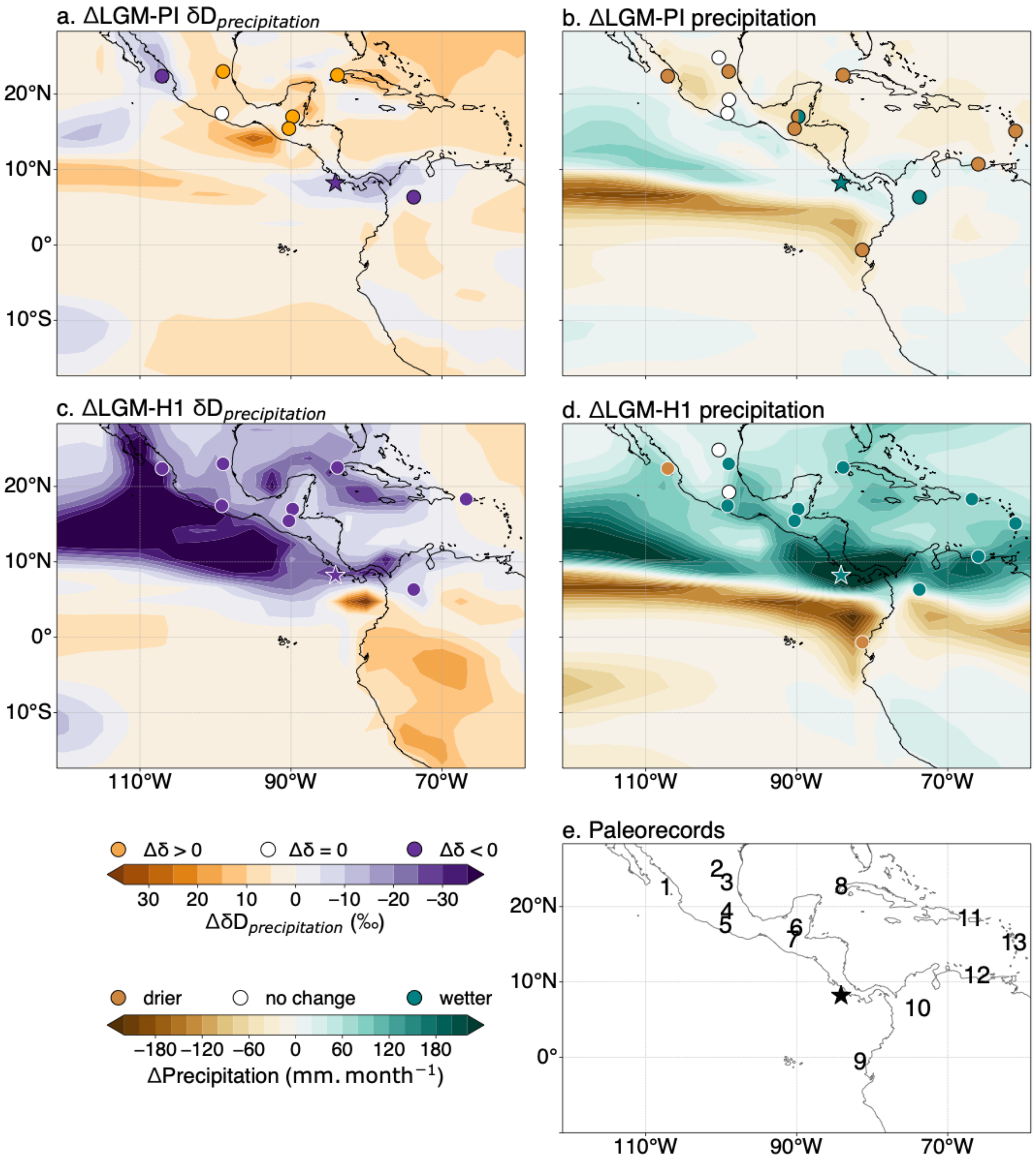

Figure 5. Synthetic map representing the extracted precipitation (b and d) and its associated δD of precipitation (a and c) as simulated by iCESM (Zhu et al., 2017) for the boreal summer (July, August and September) in the full iTrace simulation (He et al., 2021). Maps were computed for the LGM-PI (a and b) and LGM-H1 (c and d) anomalies. iTrace time intervals are defined as follows: LGM and PI control experiments from Zhu et al. (2017), H1 from 16 to 15 kyr BP iTrace (He et al., 2021). Dot colours indicate the sign of hydroclimatic changes as

reported in each original publication listed in the Supplementary Data. (e) Archives - star: MD02-2529 δD biomarker (this study); numbers: see Supplementary Data for corresponding record numbers and analyzed proxies.

To investigate how the EEP SST changes could have impacted the Panama Basin rainfall, we updated the LGM SST anomaly compilation published in Dubois et al. (2009) with the two $U^{k'}_{37}$-based SST records of Rein et al. (2005) and Bova et al. (2015) (**Figure 6**). The resulting LGM map of alkenone-based SST indicates that the gradient found between the northern EPWP and the cold tongue was enhanced during the LGM compared to the Holocene (Dubois et al., 2009, **Figure 6**). The magnitudes of the LGM cooling along the warm pool, equatorial front and cold tongue latitudinal transect are statistically distinct (t-test, p-value < 0.005).

Over the late Pleistocene, Rincón-Martínez et al. (2010) found decreased riverine runoff during glacials along the Ecuadorian margin where rainfall occurs during austral summer nowadays, that were concomitant with increases in the meridional and zonal SST gradients along the Equatorial Pacific. They attributed these precipitation increases to a northward ITCZ shift induced by strong cooling periods along the Peruvian-Humboldt current system as a whole, which acted to push the ITCZ further away from the equatorial front in the EEP (Rincón-Martínez et al., 2010). In such a scenario, an increased SST gradient results in an increased precipitation gradient in the EEP. This mechanism would explain why core MD02-2529, situated immediately North of the modern-day precipitation maximum that occurs above Panama Basin, received more rainfall in response to an ITCZ northward shift.

5.4.2 Ocean-atmosphere interactions in model simulations

We now test whether such a mechanism is at work in the PMIP4 models by considering the LGM and PI simulations (Kageyama et al., 2021). The PMIP4 multi-model ensemble shows a decrease in LGM precipitation in all high precipitation areas, including the EEP (see Figure 6 in Kageyama et al., 2021). However, a local response of the ITCZ induced by a regional SST pattern is difficult to capture in oceanic models that already struggle to simulate the modern equatorial thermocline, which also has implications for the long-standing double ITCZ bias (Zhu et al., 2021b). Another source of model bias is the resolution of the orographic height in different models, which changes the modelled climatology and the resulting regional SST, also contributing to the double ITCZ bias in the EEP (Baldwin et al., 2021).

We investigate the ocean-atmosphere coupling in each individual PMIP4 LGM model output to see whether, in the diversity of inter-model responses, we could detect the mechanism we invoke (**Figure 6**). The set comprises thirteen LGM-PI SST and precipitation anomalies as simulated by twelve models included in PMIP4 (Kageyama et al., 2021), and CESM2.1, which implements the PMIP4 protocol (Zhu et al., 2021a). Based on individual models, there is no agreement regarding the spatial distribution and the sign of changes in inter-model precipitation anomalies (**Figure 6**). Over the thirteen models, two models exhibit a clear pattern of LGM precipitation increase along the Pacific coast of Central America (CCSM4, CESM2.1). Five do not really show a clear pattern (MIROC, HadCM3 ICE-6G, CESM1.2, AWIESM1 and AWIESM2), with patches of slightly more or less precipitation over Central America. The remaining six models (HadCM3 GLAC-1D, INM-CM4-8, iLOVECLIM GLAC-1D, iLOVECLIM ICE-6G, MPI-ESM1.2 and IPSL-CM5A2) show mainly an LGM drying anomaly. For most of the models though, when the LGM SST is marked by a pronounced regional cooling along the equator, there is a decrease in precipitation in the immediate northern vicinity of the cold tongue (**Figure 6**), suggesting that despite a vast range of regional rainfall patterns for the LGM, similar ocean-atmosphere interactions were at play.

Regional air-sea interactions of an air parcel blowing north across the cold tongue frontal zone explain that the specific humidity in the frontal region just north of the cold tongue is relatively dry (Thum et al., 2002). As this northward-moving dry air parcel warms with a lag relative to the underlying SST, it eventually becomes laden with moisture further north, and latent heat transport occurs where the wind blows above the EPWP, i.e. north of the dry region (Thum et al., 2002). Once waterlogged, the air parcel initiates intense precipitation during the boreal summer when it reaches the ITCZ (**Figure 1e**, see also **Figure S2** for wind vectors).

The SST and precipitation differences between the LGM and PI (see Methods and **Figure 6** for calculation) show that there is a significant positive linear relationship between the SST gradient between the EPWP and the cold tongue and the precipitation gradient between a north ITCZ position and a south ITCZ position (**Figure 7**). In particular, models that simulate the strong LGM cooling in the cold tongue (i.e. high SST gradient) are those that correctly simulate an intensification of precipitation in the vicinity of the MD02-2529 core (**Figure 7**). Models that instead simulate no LGM cooling (or even LGM warming) in the cold tongue (i.e. low SST gradient) are those that simulate a decrease in precipitation (**Figure 7**). This mechanism illustrates the regional influence of SST on the ITCZ.

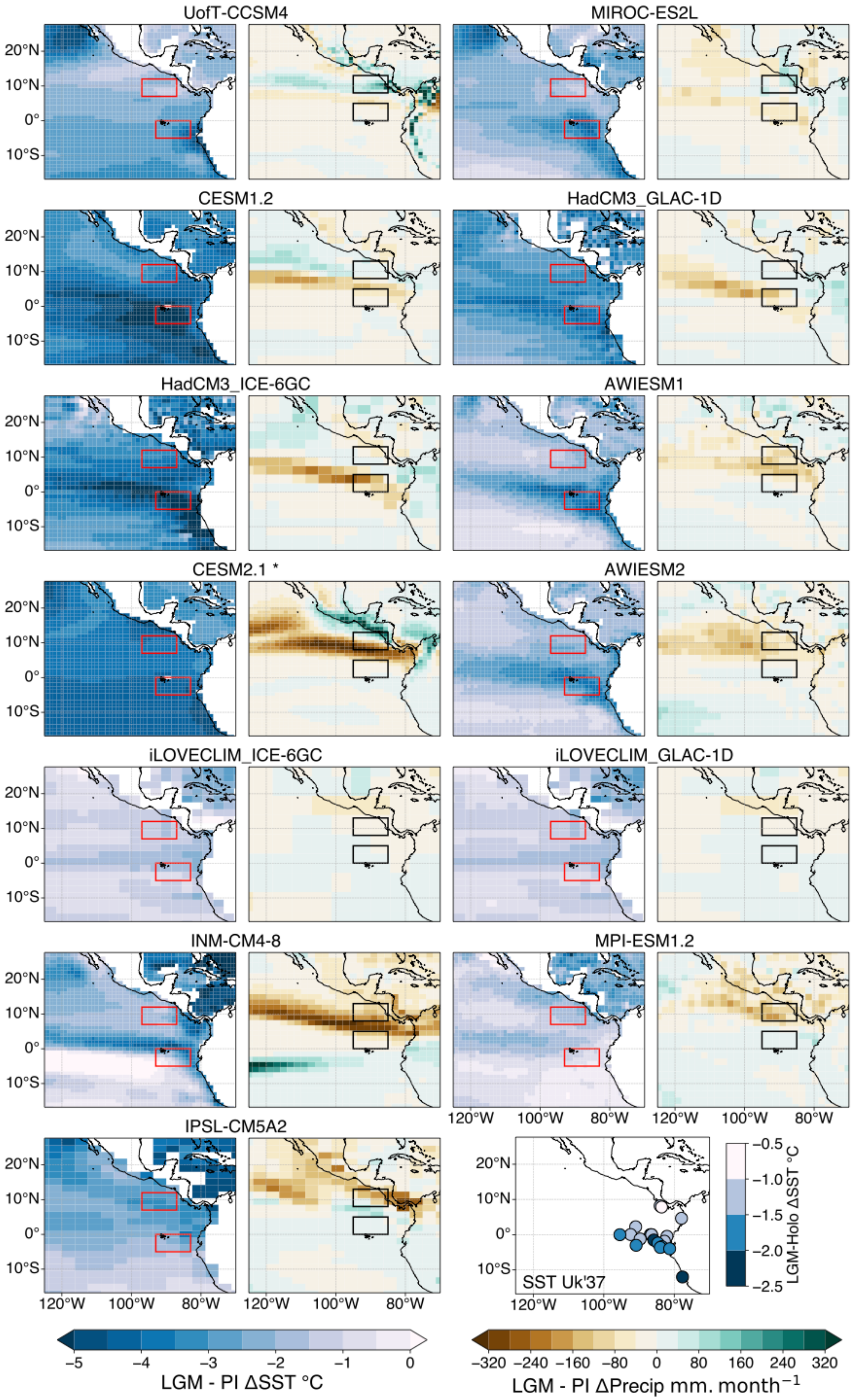
UofT-CCSM4
MIROC-ES2L
CESM1.2
HadCM3_GLAC-1D
HadCM3_ICE-6GC
AWIESM1
CESM2.1 *
AWIESM2
iLOVECLIM_ICE-6GC
iLOVECLIM_GLAC-1D
INM-CM4-8
MPI-ESM1.2
IPSL-CM5A2
20°N
10°N
0°
10°S
120°W
100°W
80°W
SST Uk'37
−0.5
−1.0
−1.5
−2.0
−2.5
LGM-Holo ΔSST °C
−5
−4
−3
−2
−1
0
LGM - PI ΔSST °C
−320
−240
−160
−80
0
80
160
240
320
LGM - PI ΔPrecip mm. month−1

Figure 6. LGM - PI anomalies of summer (July, August, September) SST (°C) and precipitation (mm.month^{-1}), as simulated by PMIP4 models (described in Kageyama et al., 2021 and Zhu et al., 2021a for CESM2.1). Note that SST anomalies are divided by 2 for CESM2.1 to avoid color saturation since there is an SST cooling bias reported in the model (Zhu et al., 2021a). Rectangles represent the delimited area used for SST (red) and precipitation (black) gradient calculation in **Figure 7**. The last bottom right panel shows $U^{k'}_{37}$-based SST LGM-Holocene anomalies compilation from Dubois et al. 2009, updated with two Uk'_{37}-based SST records (Rein et al., 2005; Bova et al., 2015). Note that the grid size shows the accurate resolution and the high spatial disparity between the models.

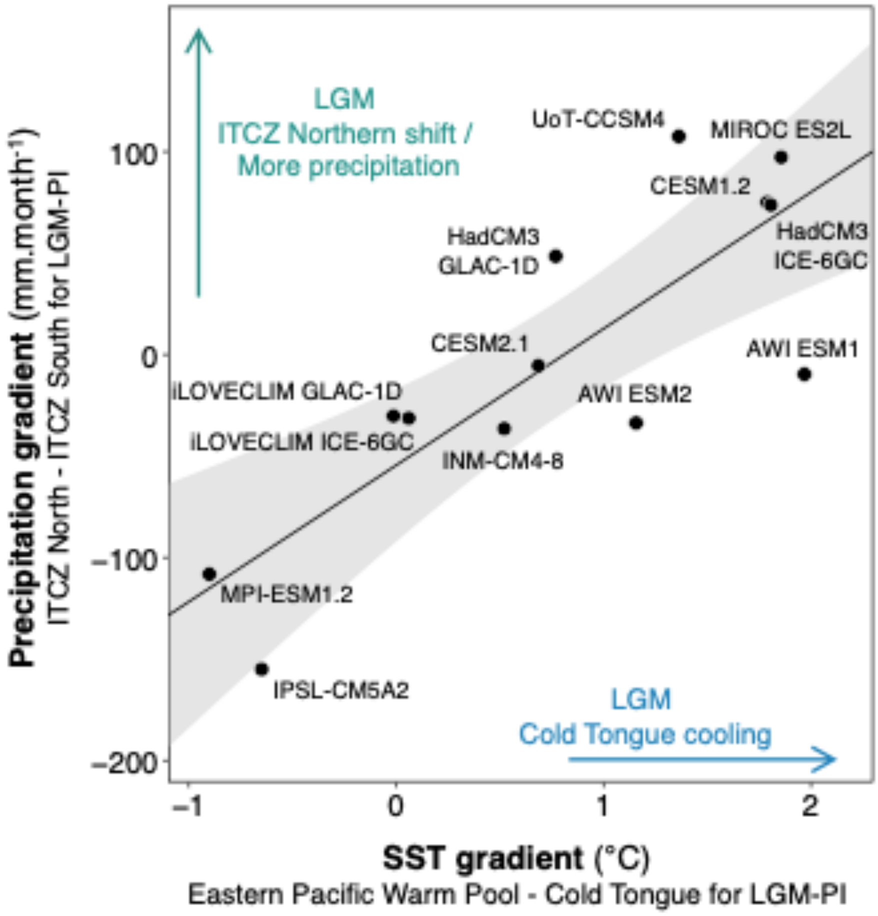

Figure 7. Correlation between the EEP ΔSST gradient (between the cold tongue and the warm pool for the LGM in comparison to the PI, red rectangles **Figure 6**) and the

EEP/Central America ΔPrecipitation (between the precipitation area of the Northern position of the ITCZ and Southern position of the ITCZ for the LGM in comparison to the PI, black rectangles, **Figure 6**). 12 PMIP4 models (Kageyama et al., 2021) are plotted along with CESM2.1 (Zhu et al., 2021a). Black line represents the linear regression and the grey area represents the 95% confidence interval on the regression (R^2=0.6794, p-value=0.0005289). Values were extracted and averaged for summer (July, August, September) in a 10° longitude x 5° latitude area (red and black rectangles in **Figure 6**, refer to Supplementary Data for extracted values).

6 Conclusion

We used δD of *n*-alkanes extracted from the MD02-2529 marine sediment core to infer precipitation changes above southern Central America during the last 56 kyr. We report a wet LGM co-occurring with an intensified cold-tongue cooling, suggesting that the southern Central America rainfall changes intimately co-vary with the SST equatorial cold front strength in the EEP. Following the LGM, we report on a progressive drying trend towards the Holocene occurring during the H1. The drying trend recorded during the H1 event is consistent with the regional and global hydroclimate response to a southern shift of the ITCZ. However, the temporal complexity of the regional hydroclimate response to the H1 still requires further study.

We use LGM PMIP4 simulations to better understand how regional EEP oceanic specificities lead to wetter conditions in southern Central America. We identify a mechanism that involves a tight ocean-atmosphere coupling in which the strength of the equatorial oceanic temperature front directly impacts the ITCZ position, regardless of the sign of latitudinal SST and precipitation gradients simulated by the individual models.

Furthermore, our results have implications for evaluating the models' abilities to accurately reproduce past changes in low-latitude precipitation. Studies comparing multi-model extracted data must exercise caution and use a regional approach to both highlight regional climatic processes and overcome methodological bias arising from the diversity of model resolutions. Finally, the accuracy in the representation of frontal zones along the equator in paleoclimate simulations appears to be crucial to faithfully reproduce the associated pattern of tropical rainfall changes. Those features need to be considered for future projections.

Data availability

MD02-2529 *n*-alkanes data will be uploaded to an online database. The ERA5 datasets are available at https://doi.org/10.24381/cds.6860a573. The iTraCE datasets are available at https://www.earthsystemgrid.org/dataset/ucar.cgd.ccsm4.iTRACE.html. PMIP4 SST and precipitation monthly model outputs were retrieved from the following database http://dods.lsce.ipsl.fr/pmip4/db/ maintained by Jean-Yves Peterschmitt, LSCE. This database was partly created based on ESGF simulations cited in Kageyama et al., 2021. In particular, the PMIP4-CMIP6 LGM and associated piControl simulations have the associated DOIs: AWI-ESM-1-1-LR: https://doi.org/10.22033/ESGF/CMIP6.9330 and https://doi.org/10.22033/ESGF/CMIP6.9335; INM-CM4-8: https://doi.org/10.22033/ESGF/CMIP6.5075 and https://doi.org/10.22033/ESGF/CMIP6.5080; MIROC-ES2L: https://doi.org/10.22033/ESGF/CMIP6.5644 and https://doi.org/10.22033/ESGF/CMIP6.5710; MPI-ESM1-2-LR: https://doi.org/10.22033/ESGF/CMIP6.6642 and https://doi.org/10.22033/ESGF/CMIP6.6675

Acknowledgements

We thank the anonymous referees for valuable suggestions. We thank financial support from the CNRS INSU-LEFE CHEMICAL project and the ANR ISOBIOCLIM. We acknowledge the CESM Project and CISL supercomputing resources regarding the use of iTrace simulations

(He et al., 2021). The authors would like to thank all the modelling groups who provided the PMIP4 output for this analysis, WCRP, CMIP panel, PCMDI, ESGF infrastructures for sharing data, WCRP and CLIVAR for supporting the PMIP project.

References

Aggarwal, P.K., Romatschke, U., Araguas-Araguas, L., Belachew, D., Longstaffe, F.J., Berg, P., Schumacher, C., Funk, A., 2016. Proportions of convective and stratiform precipitation revealed in water isotope ratios. Nature Geosci 9, 624–629. https://doi.org/10.1038/ngeo2739

Alvarez-Solas, J., Charbit, S., Ritz, C., Paillard, D., Ramstein, G., Dumas, C., 2010. Links between ocean temperature and iceberg discharge during Heinrich events. Nature Geosci 3, 122–126. https://doi.org/10.1038/ngeo752

Amador, J.A., Alfaro, E.J., Lizano, O.G., Magaña, V.O., 2006. Atmospheric forcing of the eastern tropical Pacific: A review. Progress in Oceanography 69, 101–142. https://doi.org/10.1016/j.pocean.2006.03.007

Arbuszewski, J.A., deMenocal, P.B., Cléroux, C., Bradtmiller, L., Mix, A., 2013. Meridional shifts of the Atlantic intertropical convergence zone since the Last Glacial Maximum. Nature Geosci 6, 959–962. https://doi.org/10.1038/ngeo1961

Baldwin, J.W., Atwood, A.R., Vecchi, G.A., Battisti, D.S., 2021. Outsize Influence of Central American Orography on Global Climate. AGU Advances 2. https://doi.org/10.1029/2020AV000343

Bard, E., Rostek, F., Turon, J.-L., Gendreau, S., 2000. Hydrological Impact of Heinrich Events in the Subtropical Northeast Atlantic. Science 289, 1321–1324. https://doi.org/10.1126/science.289.5483.1321

Beaufort, L., 2002. Les rapports de campagne à la mer, MD126/MONA-IMAGESVIII.

Bova, S.C., Herbert, T., Rosenthal, Y., Kalansky, J., Altabet, M., Chazen, C., Mojarro, A., Zech, J., 2015. Links between eastern equatorial Pacific stratification and atmospheric CO 2 rise during the last deglaciation. Paleoceanography 30, 1407–1424. https://doi.org/10.1002/2015PA002816

Braconnot, P., Harrison, S.P., Kageyama, M., Bartlein, P.J., Masson-Delmotte, V., Abe-Ouchi, A., Otto-Bliesner, B., Zhao, Y., 2012. Evaluation of climate models using palaeoclimatic data. Nature Clim Change 2, 417–424. https://doi.org/10.1038/nclimate1456

Bradley, R.S., Diaz, H.F., 2021. Late Quaternary Abrupt Climate Change in the Tropics and Sub-Tropics: The Continental Signal of Tropical Hydroclimatic Events (THEs). Reviews of Geophysics 59. https://doi.org/10.1029/2020RG000732

Brady, E., Stevenson, S., Bailey, D., Liu, Z., Noone, D., Nusbaumer, J., et al. (2019). The connected isotopic water cycle in the community Earth system model version 1. *Journal of Advances in Modeling Earth Systems*, *11*(8), 2547–2566. https://doi.org/10.1029/2019ms001663

Chelton, D.B., Esbensen, S.K., Schlax, M.G., Thum, N., Freilich, M.H., Wentz, F.J., Gentemann, C.L., McPhaden, M.J., Schopf, P.S., 2001. Observations of Coupling between Surface Wind Stress and Sea Surface Temperature in the Eastern Tropical Pacific. J. Climate 14, 1479–1498. https://doi.org/10.1175/1520-0442(2001)014<1479:OOCBSW>2.0.CO;2

Dansgaard, W., 1964. Stable isotopes in precipitation. Tellus 16, 436–468. https://doi.org/10.1111/j.2153-3490.1964.tb00181.x

Douglas, P.M.J., Pagani, M., Brenner, M., Hodell, D.A., Curtis, J.H., 2012. Aridity and vegetation composition are important determinants of leaf-wax δD values in southeastern Mexico and Central America. Geochimica et Cosmochimica Acta 97, 24–45. https://doi.org/10.1016/j.gca.2012.09.005

Douville, H., K. Raghavan, J. Renwick, R.P. Allan, P.A. Arias, M. Barlow, R. Cerezo-Mota, A. Cherchi, T.Y. Gan, J. Gergis, D. Jiang, A. Khan, W. Pokam Mba, D. Rosenfeld, J. Tierney, and O. Zolina, 2021: Water Cycle Changes. In Climate Change 2021: The Physical Science Basis. Contribution of Working Group I to the Sixth Assessment Report of the Intergovernmental Panel on Climate Change [Masson-Delmotte, V., P. Zhai, A. Pirani, S.L. Connors, C. Péan, S. Berger, N. Caud, Y. Chen, L. Goldfarb, M.I. Gomis, M. Huang, K. Leitzell, E. Lonnoy, J.B.R. Matthews, T.K. Maycock, T. Waterfield, O. Yelekçi, R. Yu, and B. Zhou (eds.)]. Cambridge University Press, Cambridge, United Kingdom and New York, NY, USA, pp. 1055–1210, https://doi:10.1017/9781009157896.010

Dubois, N., Kienast, M., Normandeau, C., Herbert, T.D., 2009. Eastern equatorial Pacific cold tongue during the Last Glacial Maximum as seen from alkenone paleothermometry. Paleoceanography 24, 2009PA001781. https://doi.org/10.1029/2009PA001781

Durán-Quesada, A.M., Gimeno, L., Amador, J.A., Nieto, R., 2010. Moisture sources for Central America: Identification of moisture sources using a Lagrangian analysis technique. J. Geophys. Res. 115, D05103. https://doi.org/10.1029/2009JD012455

Geen, R., Bordoni, S., Battisti, D.S., Hui, K., 2020. Monsoons, ITCZs, and the Concept of the Global Monsoon. Reviews of Geophysics 58, e2020RG000700. https://doi.org/10.1029/2020RG000700

Harris, R.N., Sakaguchi, A., Petronotis, K., Baxter, A.T., Berg, R., Burkett, A., Charpentier, D., Choi, J., Diz Ferreiro, P., Hamahashi, M., Hashimoto, Y., Heydolph, K., Jovane, L., Kastner, M., Kurz, W., Kutterolf, S.O., Li, Y., Malinverno, A., Martin, K.M., Millan, C., Nascimento, D.B., Saito, S., Sandoval Gutierrez, M.I., Screaton, E.J., Smith-Duque, C.E., Solomon, E.A., Straub, S.M., Tanikawa, W., Torres, M.E., Uchimura, H., Vannucchi, P., Yamamoto, Y., Yan, Q., and Zhao, X., 2013. Expedition 344 summary. In Harris, R.N., Sakaguchi, A., Petronotis, K., and the Expedition 344 Scientists, Proc. IODP, 344: College Station, TX (Integrated Ocean Drilling Program). https://doi:10.2204/iodp.proc.344.101.2013

He, C., Liu, Z., Otto-Bliesner, B. L., Brady, E. C., Zhu, C., Tomas, R., Clark, P. U., Zhu, J., Jahn, A., &Gu, S. (2021), Hydroclimate footprint of pan-Asian monsoon water isotope during the last deglaciation, Science Advances, 7(4), eabe2611.

Heaton, T.J., Köhler, P., Butzin, M., Bard, E., Reimer, R.W., Austin, W.E.N., Bronk Ramsey, C., Grootes, P.M., Hughen, K.A., Kromer, B., Reimer, P.J., Adkins, J., Burke, A., Cook, M.S., Olsen, J., Skinner, L.C., 2020. Marine20—The Marine Radiocarbon Age Calibration Curve (0–55,000 cal BP). Radiocarbon 62, 779–820. https://doi.org/10.1017/RDC.2020.68

Hersbach, H., Bell, B., Berrisford, P., Biavati, G., Horányi, A., Muñoz Sabater, J., Nicolas, J., Peubey, C., Radu, R., Rozum, I., Schepers, D., Simmons, A., Soci, C., Dee, D., Thépaut, J-N., 2023. ERA5 monthly averaged data on pressure levels from 1940 to present. Copernicus Climate Change Service (C3S) Climate Data Store (CDS), https://doi.org/10.24381/cds.6860a573 (Accessed on 09-03-2024)

Hodell, D.A., Anselmetti, F.S., Ariztegui, D., Brenner, M., Curtis, J.H., Gilli, A., Grzesik, D.A., Guilderson, T.J., Müller, A.D., Bush, M.B., 2008. An 85-ka record of climate change in lowland Central America. Quaternary Science Reviews 27, 1152–1165. https://doi.org/10.1016/j.quascirev.2008.02.008

Huguet, C., Kim, J.-H., González-Arango, C., Ramírez-Valencia, V., Kang, S., Gal, J.-K., Shin, K.-H., 2019. Sources of organic matter in two contrasting tropical coastal environments: The Caribbean Sea and the eastern Pacific. Journal of South American Earth Sciences 96, 102349. https://doi.org/10.1016/j.jsames.2019.102349

IAEA/WMO, 2024. Global Network of Isotopes in Precipitation. The GNIP Database. Accessible at: https://nucleus.iaea.org/wiser

Kageyama, M., Albani, S., Braconnot, P., Harrison, S.P., Hopcroft, P.O., Ivanovic, R.F., Lambert, F., Marti, O., Peltier, W.R., Peterschmitt, J.-Y., Roche, D.M., Tarasov, L., Zhang, Xu, Brady, E.C., Haywood, A.M., LeGrande, A.N., Lunt, D.J., Mahowald, N.M., Mikolajewicz, U., Nisancioglu, K.H., Otto-Bliesner, B.L., Renssen, H., Tomas, R.A., Zhang, Q., Abe-Ouchi, A., Bartlein, P.J., Cao, J., Li, Q., Lohmann, G., Ohgaito, R., Shi, X., Volodin, E., Yoshida, K., Zhang, Xiao, Zheng, W., 2017. The PMIP4 contribution to CMIP6 – Part 4: Scientific objectives and experimental design of the PMIP4-CMIP6 Last Glacial Maximum experiments and PMIP4 sensitivity experiments. Geosci. Model Dev. 10, 4035–4055. https://doi.org/10.5194/gmd-10-4035-2017

Kageyama, M., Harrison, S.P., Kapsch, M.-L., Lofverstrom, M., Lora, J.M., Mikolajewicz, U., Sherriff-Tadano, S., Vadsaria, T., Abe-Ouchi, A., Bouttes, N., Chandan, D., Gregoire, L.J., Ivanovic, R.F., Izumi, K., LeGrande, A.N., Lhardy, F., Lohmann, G., Morozova, P.A., Ohgaito, R., Paul, A., Peltier, W.R., Poulsen, C.J., Quiquet, A., Roche, D.M., Shi, X., Tierney, J.E., Valdes, P.J., Volodin, E., Zhu, J., 2021. The PMIP4 Last Glacial Maximum experiments: preliminary results and comparison with the PMIP3 simulations. Clim. Past 17, 1065–1089. https://doi.org/10.5194/cp-17-1065-2021

Konecky, B.L., Noone, D.C., Cobb, K.M., 2019. The Influence of Competing Hydroclimate Processes on Stable Isotope Ratios in Tropical Rainfall. Geophysical Research Letters 46, 1622–1633. https://doi.org/10.1029/2018GL080188

Kusch, S., Eglinton, T.I., Mix, A.C., Mollenhauer, G., 2010. Timescales of lateral sediment transport in the Panama Basin as revealed by radiocarbon ages of alkenones, total organic carbon and foraminifera. Earth and Planetary Science Letters 290, 340–350. https://doi.org/10.1016/j.epsl.2009.12.030

Lachniet, M.S., Asmerom, Y., Bernal, J.P., Polyak, V.J., Vazquez-Selem, L., 2013. Orbital pacing and ocean circulation-induced collapses of the Mesoamerican monsoon over the past

22,000 y. Proc. Natl. Acad. Sci. U.S.A. 110, 9255–9260. https://doi.org/10.1073/pnas.1222804110

Lachniet, M.S., Johnson, L., Asmerom, Y., Burns, S.J., Polyak, V., Patterson, W.P., Burt, L., Azouz, A., 2009. Late Quaternary moisture export across Central America and to Greenland: evidence for tropical rainfall variability from Costa Rican stalagmites. Quaternary Science Reviews 28, 3348–3360. https://doi.org/10.1016/j.quascirev.2009.09.018

Lachniet, M.S., Patterson, W.P., 2009. Oxygen isotope values of precipitation and surface waters in northern Central America (Belize and Guatemala) are dominated by temperature and amount effects. Earth and Planetary Science Letters 284, 435–446. https://doi.org/10.1016/j.epsl.2009.05.010

Lachniet, M.S., Patterson, W.P., Burns, S., Asmerom, Y., Polyak, V., 2007. Caribbean and Pacific moisture sources on the Isthmus of Panama revealed from stalagmite and surface water δ18O gradients. Geophys. Res. Lett. 34, L01708. https://doi.org/10.1029/2006GL028469

Ladd, S.N., Maloney, A.E., Nelson, D.B., Prebble, M., Camperio, G., Sear, D.A., Hassall, J.D., Langdon, P.G., Sachs, J.P., Dubois, N., 2021. Leaf Wax Hydrogen Isotopes as a Hydroclimate Proxy in the Tropical Pacific. J Geophys Res Biogeosci 126. https://doi.org/10.1029/2020JG005891

Leduc, G., Vidal, L., Tachikawa, K., Rostek, F., Sonzogni, C., Beaufort, L., Bard, E., 2007. Moisture transport across Central America as a positive feedback on abrupt climatic changes. Nature 445, 908–911. https://doi.org/10.1038/nature05578

Leduc, G., Vidal, L., Tachikawa, K., Bard, E., 2010. Changes in Eastern Pacific ocean ventilation at intermediate depth over the last 150kyrBP. Earth and Planetary Science Letters 298, 217–228. https://doi.org/10.1016/j.epsl.2010.08.002

Linsley, B.K., Dunbar, R.B., Wellington, G.M., Mucciarone, D.A., 1994. A coral-based reconstruction of Intertropical Convergence Zone variability over Central America since 1707. J. Geophys. Res. 99, 9977. https://doi.org/10.1029/94JC00360

Liu, J., Zhao, J., He, D., Huang, X., Jiang, C., Yan, H., Lin, G., An, Z., 2022. Effects of plant types on terrestrial leaf wax long-chain n-alkane biomarkers: Implications and paleoapplications. Earth-Science Reviews 235, 104248. https://doi.org/10.1016/j.earscirev.2022.104248

Lucia, G., Zanchettin, D., Winter, A., Cheng, H., Rubino, A., Vásquez, O.J., Bernal, J.P., Cu-Xi, M., Lachniet, M.S., 2024. Atlantic Ocean thermal forcing of Central American rainfall over 140,000 years. Nat Commun 15, 10586. https://doi.org/10.1038/s41467-024-54856-0

McGee, D., Donohoe, A., Marshall, J., Ferreira, D., 2014. Changes in ITCZ location and cross-equatorial heat transport at the Last Glacial Maximum, Heinrich Stadial 1, and the mid-Holocene. Earth and Planetary Science Letters 390, 69–79. https://doi.org/10.1016/j.epsl.2013.12.043

McInerney, F.A., Helliker, B.R., Freeman, K.H., 2011. Hydrogen isotope ratios of leaf wax n-alkanes in grasses are insensitive to transpiration. Geochimica et Cosmochimica Acta 75, 541–554. https://doi.org/10.1016/j.gca.2010.10.022

Poveda, G., Mesa, O.J., 2000. On the existence of Lloró (the rainiest locality on Earth): Enhanced ocean-land-atmosphere interaction by a low-level jet. Geophysical Research Letters 27, 1675–1678. https://doi.org/10.1029/1999GL006091

Ramirez, V.M., Cruz, F.W., Vuille, M., Novello, V.F., Stríkis, N.M., Cheng, H., Zhang, H.W., Bernal, J.P., Du, W.J., Ampuero, A., Deininger, M., Chiessi, C.M., Tejedor, E., Campos, J.L., Ait Brahim, Y., Edwards, R.L., 2023. Summer insolation controlled movements of Intertropical

Convergence Zone during last glacial cycle in northern South America. Commun Earth Environ 4, 495. https://doi.org/10.1038/s43247-023-01124-6

Rasmusson, E.M., Carpenter, T.H., 1982. Variations in Tropical Sea Surface Temperature and Surface Wind Fields Associated with the Southern Oscillation/El Niño. Mon. Wea. Rev. 110, 354–384. https://doi.org/10.1175/1520-0493(1982)110<0354:VITSST>2.0.CO;2

Rein, B., Lückge, A., Reinhardt, L., Sirocko, F., Wolf, A., Dullo, W., 2005. El Niño variability off Peru during the last 20,000 years. Paleoceanography 20, 2004PA001099. https://doi.org/10.1029/2004PA001099

Rincón-Martínez, D., Lamy, F., Contreras, S., Leduc, G., Bard, E., Saukel, C., Blanz, T., Mackensen, A., Tiedemann, R., 2010. More humid interglacials in Ecuador during the past 500 kyr linked to latitudinal shifts of the equatorial front and the Intertropical Convergence Zone in the eastern tropical Pacific. Paleoceanography 25. https://doi.org/10.1029/2009PA001868

Risi, C., Bony, S., Vimeux, F., 2008. Influence of convective processes on the isotopic composition (δ18O and δD) of precipitation and water vapor in the tropics: 2. Physical interpretation of the amount effect. J. Geophys. Res. 113, 2008JD009943. https://doi.org/10.1029/2008JD009943

Romero O., Leduc G., Vidal L., Fischer G., 2011. Millennial Variability and Long-term Changes of the Diatom Production in the Eastern Equatorial Pacific during the Last Glacial Cycle. Paleoceanography, 26, PA2212. https://doi.org/10.1029/2010PA002099

Sachse, D., Billault, I., Bowen, G.J., Chikaraishi, Y., Dawson, T.E., Feakins, S.J., Freeman, K.H., Magill, C.R., McInerney, F.A., van der Meer, M.T.J., Polissar, P., Robins, R.J., Sachs, J.P., Schmidt, H.-L., Sessions, A.L., White, J.W.C., West, J.B., Kahmen, A., 2012. Molecular Paleohydrology: Interpreting the Hydrogen-Isotopic Composition of Lipid Biomarkers from

Photosynthesizing Organisms. Annu. Rev. Earth Planet. Sci. 40, 221–249. https://doi.org/10.1146/annurev-earth-042711-105535

Sánchez-Murillo, R., Birkel, C., Welsh, K., Esquivel-Hernández, G., Corrales-Salazar, J., Boll, J., Brooks, E., Roupsard, O., Sáenz-Rosales, O., Katchan, I., Arce-Mesén, R., Soulsby, C., Araguás-Araguás, L.J., 2016. Key drivers controlling stable isotope variations in daily precipitation of Costa Rica: Caribbean Sea versus Eastern Pacific Ocean moisture sources. Quaternary Science Reviews 131, 250–261. https://doi.org/10.1016/j.quascirev.2015.08.028

Sánchez-Murillo, R., Esquivel-Hernández, G., Welsh, K., Brooks, E.S., Boll, J., Alfaro-Solís, R., Valdés-González, J., 2013. Spatial and Temporal Variation of Stable Isotopes in Precipitation across Costa Rica: An Analysis of Historic GNIP Records. Open Journal of Modern Hydrology 03, 226–240. https://doi.org/10.4236/ojmh.2013.34027

Sánchez-Murillo, R., Durán-Quesada, A.M., Birkel, C., Esquivel-Hernández, G., Boll, J., 2017. Tropical precipitation anomalies and d -excess evolution during El Niño 2014-16. Hydrol. Process. 31, 956–967. https://doi.org/10.1002/hyp.11088

Sauer, P.E., Eglinton, T.I., Hayes, J.M., Schimmelmann, A., Sessions, A.L., 2001. Compound-specific D/H ratios of lipid biomarkers from sediments as a proxy for environmental and climatic conditions. Geochimica et Cosmochimica Acta 65, 213–222. https://doi.org/10.1016/S0016-7037(00)00520-2

Schneider, T., Bischoff, T., Haug, G.H., 2014. Migrations and dynamics of the intertropical convergence zone. Nature 513, 45–53. https://doi.org/10.1038/nature13636

Sessions, A.L., Burgoyne, T.W., Hayes, J.M., 2001. Correction of H3+ Contributions in Hydrogen Isotope Ratio Monitoring Mass Spectrometry. Anal. Chem. 73, 192–199. https://doi.org/10.1021/ac000489e

Singarayer, J.S., Valdes, P.J., Roberts, W.H.G., 2017. Ocean dominated expansion and contraction of the late Quaternary tropical rainbelt. Sci Rep 7, 9382. https://doi.org/10.1038/s41598-017-09816-8

Suh, Y.J., Diefendorf, A.F., Bowen, G.J., Cotton, J.M., Ju, S.-J., 2019. Plant wax integration and transport from the Mississippi River Basin to the Gulf of Mexico inferred from GIS-enabled isoscapes and mixing models. Geochimica et Cosmochimica Acta 257, 131–149. https://doi.org/10.1016/j.gca.2019.04.022

Svensson, A., Dahl-Jensen, D., Steffensen, J.P., Blunier, T., Rasmussen, S.O., Vinther, B.M., Vallelonga, P., Capron, E., Gkinis, V., Cook, E., Kjær, H.A., Muscheler, R., Kipfstuhl, S., Wilhelms, F., Stocker, T.F., Fischer, H., Adolphi, F., Erhardt, T., Sigl, M., Landais, A., Parrenin, F., Buizert, C., McConnell, J.R., Severi, M., Mulvaney, R., Bigler, M., 2020. Bipolar volcanic synchronization of abrupt climate change in Greenland and Antarctic ice cores during the last glacial period. Clim. Past 16, 1565–1580. https://doi.org/10.5194/cp-16-1565-2020

Tharammal, T., Bala, G., Noone, D., 2017. Impact of deep convection on the isotopic amount effect in tropical precipitation. J. Geophys. Res. Atmos. 122, 1505–1523. https://doi.org/10.1002/2016JD025555

Thum, N., Esbensen, S.K., Chelton, D.B., McPhaden, M.J., 2002. Air–Sea Heat Exchange along the Northern Sea Surface Temperature Front in the Eastern Tropical Pacific. J. Climate 15, 3361–3378. https://doi.org/10.1175/1520-0442(2002)015<3361:ASHEAT>2.0.CO;2

Tierney, J.E., Smerdon, J.E., Anchukaitis, K.J., Seager, R., 2013. Multidecadal variability in East African hydroclimate controlled by the Indian Ocean. Nature 493, 389–392. https://doi.org/10.1038/nature11785

Trenberth, K.E., Shea, D.J., 2005. Relationships between precipitation and surface temperature. Geophysical Research Letters 32, 2005GL022760. https://doi.org/10.1029/2005GL022760

Waelbroeck, C., Labeyrie, L., Michel, E., Duplessy, J.C., McManus, J.F., Lambeck, K., Balbon, E., Labracherie, M., 2002. Sea-level and deep water temperature changes derived from benthic foraminifera isotopic records. Quaternary Science Reviews 21, 295–305. https://doi.org/10.1016/S0277-3791(01)00101-9

Wang, C., Enfield, D.B., 2001. The Tropical Western Hemisphere Warm Pool. Geophys. Res. Lett. 28, 1635–1638. https://doi.org/10.1029/2000GL011763

Warken, S.F., Scholz, D., Spötl, C., Jochum, K.P., Pajón, J.M., Bahr, A., Mangini, A., 2019. Caribbean hydroclimate and vegetation history across the last glacial period. Quaternary Science Reviews 218, 75–90. https://doi.org/10.1016/j.quascirev.2019.06.019

Wright, K.T., Johnson, K.R., Marks, G.S., McGee, D., Bhattacharya, T., Goldsmith, G.R., Tabor, C.R., Lacaille-Muzquiz, J.-L., Lum, G., Beramendi-Orosco, L., 2023. Dynamic and thermodynamic influences on precipitation in Northeast Mexico on orbital to millennial timescales. Nat Commun 14, 2279. https://doi.org/10.1038/s41467-023-37700-9

Zhao, N., Keigwin, L.D., 2018. An atmospheric chronology for the glacial-deglacial Eastern Equatorial Pacific. Nat Commun 9, 3077. https://doi.org/10.1038/s41467-018-05574-x

Zhu, J., Liu, Z., Brady, E. C., Otto-Bliesner, B. L., Zhang, J., Noone, D., Tomas, R., Nusbaumer, J., Wong, T., Jahn, A., & Tabor, C. (2017). Reduced ENSO variability at the LGM revealed by an isotope-enabled Earth system model. *Geophysical Research Letters*, *44*(13), 6984–6992. https://doi.org/10.1002/2017GL073406

Zhu, J., Otto-Bliesner, B.L., Brady, E.C., Poulsen, C.J., Tierney, J.E., Lofverstrom, M., DiNezio, P., 2021a. Assessment of Equilibrium Climate Sensitivity of the Community Earth

System Model Version 2 Through Simulation of the Last Glacial Maximum. Geophysical Research Letters 48, e2020GL091220. https://doi.org/10.1029/2020GL091220

Zhu, Y., Zhang, R.-H., Li, D., Chen, D., 2021b. The Thermocline Biases in the Tropical North Pacific and Their Attributions. Journal of Climate 34, 1635–1648. https://doi.org/10.1175/JCLI-D-20-0675.1